Measurements of the Turbulent Boundary Layer under Pack Ice

MILES G. MCPHEE[1] AND J. DUNGAN SMITH

Department of Geophysics, University of Washington, Seattle 98195

(Manuscript received 19 December 1975, in revised form 7 May 1976)

ABSTRACT

The mean and turbulent flow structure under pack ice was measured during the 1972 AIDJEX pilot study with small mechanical current meter triplets at eight levels in the planetary boundary layer. CTD profiles showed a well-mixed layer of nearly neutral stability to about 35 m, bounded below by a strong pycnocline. The skin friction velocity u_* was determined by measuring the Reynolds stress at 2 and 4 m below the ice (beyond the surface layer) and from consideration of other terms in the mean momentum equation. Local pressure gradients and advective acceleration due to topography could not be ignored; when an estimate of the effect was included, u_* was 1.0 ± 0.1 cm s^{-1} when the ice velocity relative to the ocean was 24 cm s^{-1}.

With the proper coordinate transformation, the planetary boundary layer of the ocean resembles that of the atmosphere. Composite averages of non-dimensional Reynolds stress and mean flow in the ocean, when compared with recent models of a neutrally buoyant, horizontally homogeneous atmosphere, fit the model predictions fairly well. However, the lateral component (perpendicular to surface stress) departed markedly from those predictions, indicating that form drag associated with pressure ridge keels is important.

Peaks in spectra of vertical velocity were used to estimate eddy viscosity proportional to mixing length at eight levels in the outer layer. Results agreed well with the models, but this eddy viscosity did not provide a simple relation between Reynolds stress and mean flow shear.

1. Introduction

One of the foremost problems in geophysical fluid dynamics is understanding the mechanisms by which turbulent flow in a rotating system exchanges momentum with a solid boundary. Recently the planetary boundary layer (PBL) problem has attracted interest because of the need for better answers to such questions as how surface stress is related to the mean flow in both magnitude and direction, and what length and time scales are pertinent for turbulent transfer processes in the boundary layer. Even in the simplest steady-state, neutrally buoyant, horizontally homogeneous idealization, describing the three-way balance among a driving force, the Coriolis force and the momentum flux gradient is a formidable problem. Progress is also hampered by the difficulty in measuring turbulent flow, especially in the outer part of the boundary layer where forces are small and scales are large.

A good example of the need for accurate boundary layer theory is predicting the driving and retarding forces that act on pack ice as it responds to synoptic-scale weather systems. The wind exerts stress on the ice through the upper boundary layer and the ice in turn drives the ocean through its boundary layer. As part of a large effort to understand the dynamics of sea ice, the Arctic Ice Dynamics Joint Experiment (AIDJEX) has made detailed studies of both atmospheric and oceanic boundary layers during its pilot studies. This paper presents some results of flow and density measurements made in the upper layers of the Arctic Ocean under multi-year pack ice at the main AIDJEX camp during April 1972.

As we analyzed the ocean stress data for the AIDJEX ice model, we realized that in many respects we had a good scale model not only of the oceanic but also of the atmospheric PBL and that we could provide turbulence data that would require massive effort to obtain in the outer part of the atmosphere. The approach we have taken, then, is to present our measurements in the context of recent PBL theory developed primarily for the atmosphere.

2. Boundary layer equations

The steady Boussinesq equation for an incompressible flow of large Reynolds number in which vertical (x_3 axis) derivatives are much greater than horizontal ones and repeated indices imply summation is

$$U_j \frac{\partial}{\partial x_j} U_i + 2\omega \epsilon_{ijk} n_j U_k = -\frac{1}{\rho_0} \frac{\partial P}{\partial x_i} - \frac{\partial}{\partial z} \overline{u_i w} - g \frac{\rho'}{\rho_0} \delta_{i3}.$$

Here the instantaneous velocity has been divided into a mean part U_i and a fluctuating part u_i; ωn_j denotes the angular velocity of the earth; ρ_0 denotes the reference

[1] Present affiliation: AIDJEX, University of Washington, Seattle 98195.

density at a point, while ρ' denotes the deviation of density from its hydrostatic reference state; and δ_{ij} and ϵ_{ijk} denote the second- and third-order isotropic Cartesian tensors.

For this study it is convenient to use a reference frame moving with the mean ice velocity relative to the earth. Referring to Fig. 1 and defining $\mathbf{u}_m$ as the velocity measured with respect to the moving frame, $\mathbf{u}_R$ as the surface geostrophic flow in the ocean, and $\mathbf{u}_f$ as the true velocity with respect to the earth, yields

$$\mathbf{u}_m-\mathbf{u}_R=\mathbf{u}_f-\mathbf{u}_g.$$

As long as baroclinic effects in the mixed layer are small, $\mathbf{u}_g$ can be identified with the large-scale pressure gradient due to sea-surface slope, which can be eliminated from the momentum equation by considering the difference between the measured velocity and the mean velocity at a level near the base of the mixed layer. Dropping the subscript m for measured quantities, (1) and (2) can be combined to yield the horizontal component equations

$$\left.\begin{aligned}\frac{\partial}{\partial z}(\overline{uw})-f(V-V_R)=F_x=-\frac{1}{\rho_0}\left(\frac{\partial p}{\partial x}\right)_{\text{local}}\\ -U\frac{\partial U}{\partial x}-W\frac{\partial U}{\partial z}+\cdots\\ \frac{\partial}{\partial z}(\overline{vw})+f(U-U_R)=F_y=-\frac{1}{\rho_0}\left(\frac{\partial p}{\partial y}\right)_{\text{local}}\\ -U\frac{\partial V}{\partial x}-W\frac{\partial V}{\partial z}+\cdots\end{aligned}\right\},\quad (3)$$

where F_x and F_y reflect the effects of local inhomogeneities. The terms written explicitly on the right sides of (3) are those considered most significant when the x axis is chosen to lie in the direction of surface stress. If the surface is uniform so that $F_x=F_y=0$, Eq. (3) is analogous to the velocity defect law for the atmospheric boundary layer (Tennekes and Lumley, 1972). Thus in the highly idealized case, the oceanic and atmospheric boundary layers measured from the ice are similar if each is scaled properly.

From atmospheric measurements it is fairly well established that except for a thin layer immediately adjacent to the surface, the proper scales in a neutral, horizontally homogeneous PBL are u_* for velocity, ρu_*^2 for stress and u_*/f for length, where $u_*=(\tau_s/\rho)^{\frac{1}{2}}$ is the surface friction velocity and τ_s the surface stress (Blackadar and Tennekes, 1968). Close to the boundary, the effect of rotation becomes minor and the appropriate length scale is z_0, which reflects in some way the size of roughness elements. As the surface-friction Rossby number $\mathrm{Ro}_*=u_*/fz_0$ becomes large, it is conceptually useful to consider the boundary layer divided into two

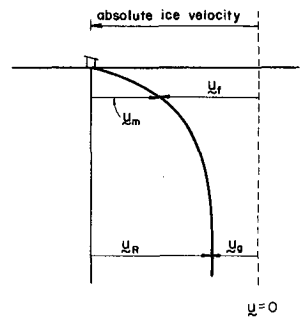

FIG. 1. Schematic of moving reference frame.

regions: an inner or surface layer and an outer or Ekman layer (Tennekes, 1973).

The relative change of stress across the surface layer is small and if the Reynolds stress $-\overline{uw}$ is related to the mean velocity gradient by an eddy viscosity (which in turn is proportional to the product of the friction velocity and the distance from the surface), the well-known "law of the wall" results. That is, if

$$-\overline{uw}=ku_*z\frac{\partial U}{\partial z}\approx u_*^2,$$

then

$$U=\frac{u_*}{k}\ln z/z_0,\quad z_0\ll z\ll u_*/f,\qquad (4)$$

where k is von Kármán's constant. Recent experiments (e.g., see Businger *et al.*, 1971) have shown that k may differ from the long-accepted constant 0.4. Tennekes (1973) attributes this to the fact that Ro_* although large for geophysical or laboratory flows, is not infinite. Where applicable in the remainder of this paper, we will use the value $k=0.35$ determined for the Kansas experiments by Businger *et al.* (1971), as it may be more representative of geophysical flows.

With the foregoing remarks in mind, it is useful to compare typical scales in the atmosphere and under the ice, as shown in Table I. The length scale in the atmosphere's outer layer is so large that it is clear why few measurements are made there. It is also obvious from the small velocity scales in the ocean that ship or mooring motion makes measurements there difficult. To our knowledge, data gathered from the ice platform during the AIDJEX series of pilot experiments represent the first simultaneous measurements of mean and turbulent velocity at several levels throughout an entire planetary boundary layer.

3. Buoyancy effects

A feature frequently observed to be a major factor in the dynamics of atmospheric boundary layers is the daily heat flux cycle during which the PBL becomes alternately stable or unstable, i.e., gravity acts to suppress or enhance vertical displacements of fluid

TABLE 1. Comparison of atmospheric (mid-latitude) and under-ice scales.

	Atmosphere	Ocean (ice-covered)
Friction velocity u_*	30 cm s^{-1}	1 cm s^{-1}
Surface layer depth	30 m	1 m
PBL depth	1000 m	35 m

parcels. Although the situation in an ice-covered oceanic boundary layer is quite different, bouyancy fluctuations may play an important role in its dynamics, and the possibility requires thorough investigation.

In general terms, the density of the Arctic Ocean, which is determined mainly by salinity, is characterized by a relatively thin (30–50 m) layer of a well-mixed water above a strong pycnocline that extends to 250–300 m. An interesting seasonal analog of the diurnal temperature fluctuations exists in the annual freezing and melting of pack ice. As water freezes at the surface, the brine that is excluded tends to sink because of its greater salinity, in much the same manner as air heated at the surface tends to rise. These effects can be compared quantitatively by introducing an Oboukov-like length scale for the ocean related to the friction velocity and the freezing rate. The horizontally homogeneous form of the turbulent energy equation (e.g., see Tennekes and Lumley, 1972) in the surface (constant flux) layer can be non-dimensionalized using kz for length and u_* for velocity to get

$$\frac{kz}{u_*^3}\overline{uw}\frac{\partial U}{\partial z}-\frac{g}{\rho_0}\frac{k}{u_*^3}\overline{\rho' wz}=\phi_D+\phi_\epsilon, \tag{5}$$

where ϕ_D is the nondimensional flux divergence and pressure transport and ϕ_ϵ the nondimensional dissipation rate. The first term on the left is the dimensionless wind shear ϕ_m and has the value $\phi_m=1$ if the law of the wall [(4)] is valid. The second term can be interpreted as the ratio $-z/L$, where

$$L=\rho_0 u_*^3/(gk\overline{\rho' w}). \tag{6}$$

By writing the energy budget (5) as

$$\phi_m-z/L=\phi_D+\phi_\epsilon, \tag{7}$$

we can characterize the contribution of buoyancy to the energy balance by the ratio $-z/L$, where L serves as a rough measure of the scale at which buoyancy production of turbulent energy becomes important relative to shear production (Tennekes and Lumley, 1972). If L is negative, there is a net downward mass flux resulting in the conversion of potential energy to turbulent kinetic energy; whereas, if it is positive, some of the turbulent kinetic energy is converted to potential energy reducing the mixing capacity of the fluid.

The rate at which mass is excluded from freezing water is equivalent to the turbulent density flux in the surface layer and is proportional to the growth rate of the ice cover, i.e.,

$$\overline{\rho' w}|_{\text{surface}}=\rho_{\text{ice}}\Delta S d/10^3, \tag{8}$$

where ΔS is the salinity difference between ice and water in parts per thousand and d is the growth rate (cm s^{-1}). From (6) we can express L in terms of growth rate as

$$L=10^3(\rho_0/\rho_{\text{ice}})[u_*^3/(gk\Delta S d)]. \tag{9}$$

Observations made by divers in the neighborhood of the experimental site in 1972 and under thick multi-year ice in previous years (Welch *et al.*, 1973) indicate that $d\approx 2\times 10^{-6}$ cm s^{-1}. With $\rho_{\text{ice}}/\rho_0\approx 0.92$, $\Delta S\approx 20‰$ and $u_*=1$ cm s^{-1}, a typical value determined in Section 7 of this paper during the period of maximum ice stress, we have

$$L\approx -400 \text{ m}.$$

In studies of the atmospheric outer layer, buoyant effects are often described by the parameter μ_*, i.e.,

$$\mu_*=\begin{cases} Z_i/L, & L<0 \text{ (unstable)} \\ u_*/fL, & L\gtrsim 0 \text{ (neutral or stable)} \end{cases}$$

where Z_i is the height of the inversion, analogous to the depth of the mixed layer (Businger and Arya, 1974; Wyngaard, *et al.*, 1974). For example $|\mu_*|=1$ implies that buoyancy is roughly as important as production of turbulent kinetic energy by shear at length scales comparable to the entire boundary layer depth.

In our case since $Z_i\approx 38$ m, we have $\mu_*\approx -0.1$, indicating that the boundary layer is very close to being neutrally stable for the storm conditions described in this paper if the stability is determined only by the surface buoyancy flux.

In addition to freezing or melting at the ice-water interface, however, stratification may be affected by processes associated with convection from open leads where the water is exposed directly to extremely low air temperatures. Smith (1974b) has discussed secondary flow patterns implied by this convection and shown evidence for such circulations in the form of jets near the ice and toward the base of the mixed layer. Of present importance is the fact that the lead-convection mechanism may act to impose a mildly stable stratification on the otherwise homogeneous wind-mixed layer. For this reason, the effects of stratification cannot be predicted solely by the Oboukov length determined from conditions at the surface. This means that although the arguments presented above can be used to preclude the possibility of significant momentum transfer by instability associated with freezing, the possibility of a stable boundary layer exists, and will be investigated in subsequent sections.

4. Planetary boundary layer models

Until recently, most efforts to solve the steady-state boundary layer equations have been aimed at relating the Reynolds stress (momentum flux) term to the mean flow shear by means of some eddy viscosity K that may depend on other parameters in the problem. Brown (1974) gives a summary of several such models.

In the last few years, new modeling techniques have been introduced that show promise of increasing our understanding of boundary layer processes significantly. Detailed description of these models is beyond the intent of this paper, but brief summaries are necessary to lay a framework in which to present measurements.

The most detailed and direct model (but also the most costly) is the three-dimensional numerical integration of the complete boundary layer equations done by Deardorff (1972). Assumptions are made about the effects of subgrid-scale motions, potential temperature replaces density in the buoyancy term, and the equations are integrated to a statistically steady state. Successful results have been published for the neutral and for several unstable cases, but not for stable regimes, apparently because subgrid-scale motions then become of major importance.

Deardorff's neutral case is bounded by a lid at $fz/u_*=0.45$, a fact which he criticizes as giving unrealistic results near the top of the layer. As we shall show, however, this height corresponds quite closely to the "lid" imposed by the pycnocline in our measurements. The model can predict fluxes of momentum, heat and passive contaminants and has become a standard against which other models are gauged for lack of actual measurements in the outer layer. Features of the model results include the following:

1) Even slight instability ($\mu_*=-1.5$) drastically reduces the lateral component in the mean wind profile.

2) Geostrophic drag (u_*/G) increases significantly with increasing instability.

3) Slight instability increases the longitudinal component of vertical momentum flux, $-\overline{uw}$, and decreases the lateral momentum flux, $-\overline{vw}$, aloft.

4) Under unstable conditions the $-\overline{uw}$ profile appears to fall off linearly to the inversion height in contrast to the neutral case in which it decreases to about zero at $fz/u_*=0.3$ and takes small negative values at greater heights.

Another class of PBL models, called second-order models, carry the mean flow equations in full and make closure assumptions for terms in the turbulence covariance equations (e.g., see Wyngaard *et al.*, 1974; Shir, 1973). These are easier to use and interpret, yet still yield detailed information predicted only crudely by the simpler K models, such as turbulent energy and momentum, heat and passive-contaminant fluxes. Wyngaard *et al.* (1974) have modeled the neutral and several unstable cases, while Shir's preliminary model is limited to the neutral PBL but allows the surface-friction Rossby number to vary.

The second-order models agree reasonably well with Deardorff's model. For the neutral layer it is found that the turbulent structure depends only weakly on the Coriolis force, so that the latitude and wind direction are not especially important except in the limiting equatorial case.

As indicated in the previous section, we did not expect an unstable layer under thick ice, but could not rule out the possibility of mild stability. Businger and Arya (1974) have recently provided a first-order (or eddy-viscosity) model that appears to give realistic wind and stress profiles for positive values of μ_*. By exploiting the fact that the log-linear profile predicted from Monin-Oboukov similarity theory for the surface layer is observed to extend some distance into the outer layer, they derive a dimensionless eddy viscosity dependent on the dimensionless height fz/u_*, and $\mu_*=u_*/fL$. The results of their model predict that increasing stability has generally opposite effects from instability, i.e., it lowers geostrophic drag, increases the turning angle between surface stress and geostrophic wind, increases stress profile curvature, and decreases the penetration distance of frictional effects.

5. The experiment

The experiment described here took place at the main camp of the 1972 AIDJEX pilot study located on a multi-year floe approximately 400 km northeast of Barrow, Alaska. AIDJEX Bulletin No. 14 contains a description of the camp (Heiberg and Bjornert, 1972) and a preliminary report on this project (Smith, 1972). Also, Smith (1974a) has reported some preliminary results from the 1972 experiment in addition to results from earlier pilot studies.

The sensors used for current measurements are small, partially ducted, mechanical current meters developed for an ongoing series of turbulent boundary layer studies in natural flows. The rotor is 1.7 cm long by 3.5 cm in diameter, with four impeller blades. Each time a reflectorized blade passes a light source in the mounting tube, it triggers two photo-diodes that combine to emit a bipolar pulse. The polarity of the leading half of the pulse determines the direction in which the rotor is turning, and the period between pulses determines the speed. The meters are carefully calibrated for head-on speed and angle-of-attack response. For the AIDJEX experiment, the threshold speed, which was governed by the electronic detection system rather than by the mechanical characteristics of the rotor, was about 2.5 cm s^{-1}. The meters were mounted as an orthogonal triplet with the (x,y) plane tilted down from the horizontal so that all components sensed enough of the mean flow to turn above threshold speed. For specifica-

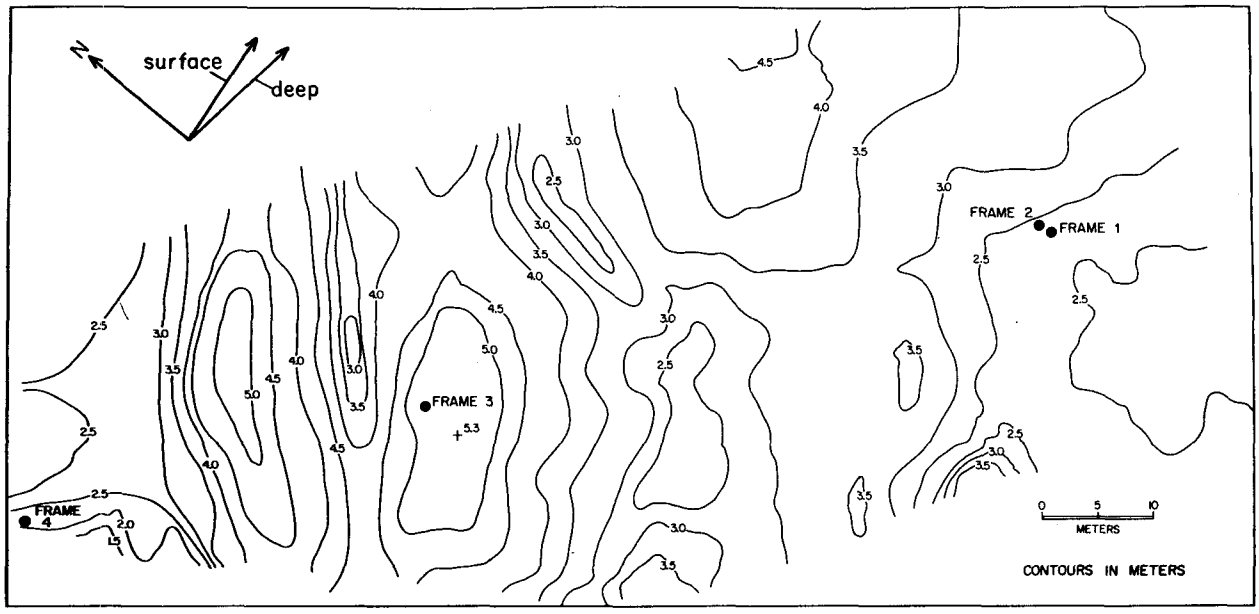

FIG. 2. Under-ice contour map of location of current meter frames. Arrows labeled "surface" and "deep" show typical current directions near the ice and at the base of the mixed layer.

tions of the meters and details of mounting see Smith (1974a).

The data collection system includes a NOVA 1200 computer, special interface and software for digitizing the current-meter periods, and tape decks for storing the data on magnetic tape. During the 1972 project, 75 channels were recorded at a sampling period of 51.2 ms. Details of the data collection and reduction are given by McPhee (1975).

The original scientific plan called for deployment of three or four frames, each carrying current meter triplets at several levels across the underside of a large pressure ridge of fairly uniform cross section, with the intent of gaging the form drag across such a feature. As it turned out, we were forced by the camp location to choose a small multi-year ridge with a maximum keel depth of only 5.3 m. Fig. 2 shows a contour map of the ice underside prepared by divers using pressure transducer measurements along a prepared grid. The contour interval is 0.5 m. To the southwest, just off the bottom of the map, lies a smoothly frozen lead that served as the camp runway. Frames 1 and 2, referred to jointly as the "main frame," were suspended beneath the instrument hut in an ice-free hole, allowing adjustment of the frames for optimum angle of attack. The main frame had current meter triplets at 11 levels to a maximum of 54 m below the ice. Frame 3 was located near the apex of the ridge and frame 4 was in smooth ice beyond the ridge; triplets on these frames were mounted at six levels to 26 m below the ice. Frames 3 and 4 were suspended from hangers frozen into the ice with a fixed orientation. This proved unfortunate since the flow direction during appreciable ice drift left one component of each triplet near or below threshold. For this reason, turbulence measurements were limited to the main frame. The mean flow at frames 3 and 4 was calculated from two components. Fig. 3 is a section drawn through the plane of the frames, showing the topographic variation to scale.

Although continuous measurements were made from 1–16 April, the period of most interest was during a storm that started early on 10 April and lasted until the morning of 14 April. All the data described herein were taken during that time, when the ice drift was typically 13–20 km day^{-1} in a steady west-northwesterly direction. In Fig. 2 the arrows attached to the north pointer indicate the relative current direction near the surface and near the base of the mixed layer. Note that the predominant flow was more parallel to the ridge than across it.

Density structure was measured with a Guildline CTD (conductivity-temperature-depth) sensor from a location about 10 m west of the main frame hut. Profiles sampled at approximately 1 m intervals down to 65 m were made several times daily. Figs. 4 and 5 show the daily mean profiles on 12 April and 13 April, each representing the average of about a dozen casts. The bars represent a sample standard deviation each way from the mean. The large variance near the surface is not well understood. In the pycnocline, variance not due to the averaging technique itself undoubtedly reflects internal wave activity and other pycnocline processes and it had its counterpart in increased variance in current velocities below the mixed layer.

The depth of minimum variance, about 35 m below

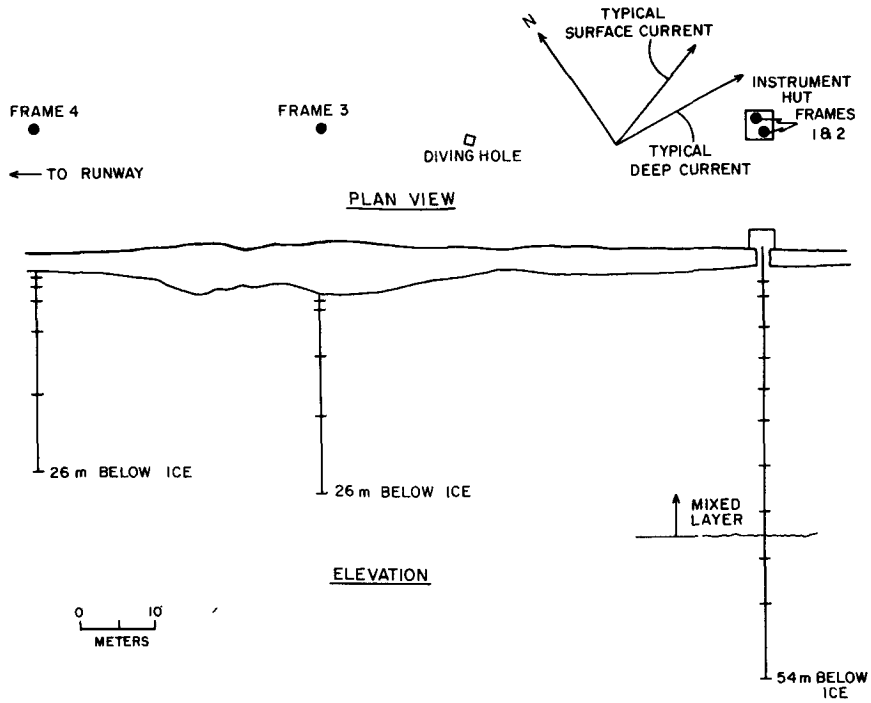

FIG. 3. Elevation in plane of current meter frames.

the ice, was taken as the depth of the mixed layer. Least-squares straight lines were fit to the mean profiles above 35 m on 12 and 13 April; both have slightly negative (stable) slopes with magnitudes of 8.8×10^{-9} and 2.1×10^{-9} gm cm^{-4}, respectively. If one presumes that the mixed layer slope persists into the surface layer and makes some assumption about a density eddy diffusivity, it can be shown that these slopes are too small to produce much buoyancy effect (McPhee, 1975). However, these arguments are not necessarily appropriate to the treatment discussed in Section 3, and we leave the question of stability until the turbulent structure of the mixed layer is discussed.

6. Current meter measurements

The coordinate system chosen for mean flow and stress calculations is oriented with the x axis parallel to the direction of surface stress, which is approximated by the relative current direction at 2 m on the main frame. The system is right-handed, with the vertical axis positive upward to conform with the development of the equations in Section 2. The Reynolds stress tensor is calculated according to

$$s_{ij}=\overline{(u_i-U_i)(u_j-U_j)}$$
$$=\frac{1}{N}\left[\sum_{k=1}^{N}u_i(k)u_j(k)-\sum_k u_i(k)\cdot\sum_k u_j(k)\right], \quad (10)$$

where N is the number of samples in the averaging time.

The concept of a stationary flow for which the time averages of pertinent properties can replace the ensemble averages assumed in most theoretical treatments of turbulence is an idealization that cannot be met in natural measurements. Any success of a statistical treatment of the current record to separate turbulence from the mean flow rests on the assumption of a spectral gap between what we term turbulence and

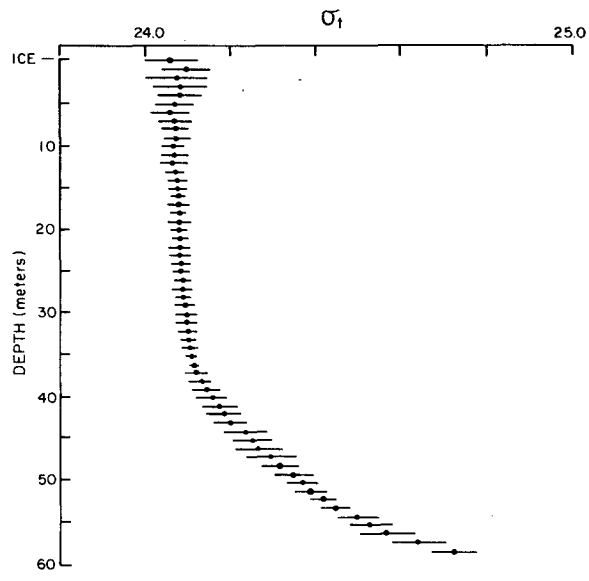

FIG. 4. Average σ_T profile from casts made on 12 April 1972. Bars represent sample standard deviations on each side of mean.

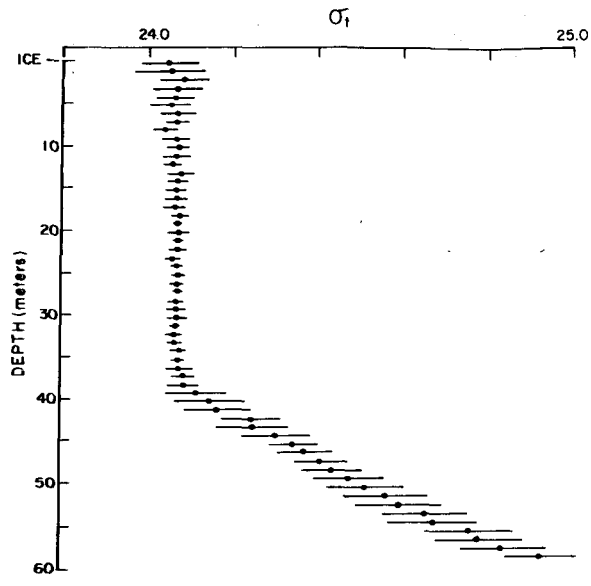

FIG. 5. As in Fig. 4 except on 13 April 1972.

other phenomena such as long gravity waves, tides, inertial motions or, in our case, independent ice motions.

There is evidence that a broad minimum exists in the area-preserving spectrum of wind speed (Monin, 1972), and we would expect the ocean to behave somewhat similarly, but the theory is not developed well enough to state clearly what relation this has to the true turbulent energy spectrum, particularly at wavenumbers low enough for anisotropic effects to be important (Tennekes and Lumley, 1972). Turbulent spectra were calculated for the data and are discussed in Section 9, but we found it more straightforward to demonstrate the presence or absence of a spectral gap by calculating stress components using different averaging times on the same data. Table 2 shows the results of one such experiment in which, for the set of numbers labeled "1 minute," we have made an average of 60 calculations performed according to (10) with N corresponding to 1 min, and so on, up to the set labeled "20 minutes," for which (10) has been calculated three times for N corresponding to 20 min. The results indicate that the change in Reynolds stress is appreciable for averaging times between 1 and 5 min; or, said another way, that turbulent features with time scales between 1 and 5 min appear to contribute significantly to the covariances, but features with scales larger than 5 min do not. At a mean advective velocity of about 20 cm s^{-1}, a "5 minute" feature has a length scale of about 6 m. We settled on an averaging interval of 20 min because of several tests like those shown in Table 2 and because it was convenient in terms of recorded file lengths in the source data.

Following arguments advanced by Wyngaard (1973), in the context of averaging times for the unstable PBL, we might expect the averaging time for stress to be several times that for turbulent kinetic energy if all the terms in the covariance equations respond basically to the same integral time scale. We found this to be qualitatively true by looking at successive 20 min averages (i.e., while the variance from average to average did not change radically, the stress components $\overline{uw}$ and $\overline{vw}$ often did). In order to minimize this uncertainty, we searched the current record for a long stretch of reasonably steady currents and made composite profiles from as many 20 min segments as that portion contained.

Fig. 6 shows measured speed and streamline bearing at two depths for 12 April. The dots show smoothed data from the acoustic bottom reference (ABR) system that represent the apparent speed and bearing of a point on the sea floor relative to the ice. We show the current record from 54 m, well into the pycnocline, to demonstrate the increase in activity observed there compared with 32 m, which is still within the mixed layer. The time segment labeled "composite averages" starting at about 1230 AST denotes the time considered best for current measurements in terms of maximum speed and steadiness. Mean flow, turbulent energy and stress components were calculated for each of fifteen 20 min intervals during this period; then these results were averaged to arrive at composite profiles (Table 3), which became the primary data set for the project. A second composite was formed for 8 h of data taken on 11 April, during which the currents were slower but essentially in the same direction. These calculations are shown in Table 4.

TABLE 2. Effects of different Reynolds stress averaging times for same 1 h segment of data.

Depth (m)	Averaging time: 1 minute $-\overline{uw}$	1 minute $-\overline{vw}$	5 minutes $-\overline{uw}$	5 minutes $-\overline{vw}$	10 minutes $-\overline{uw}$	10 minutes $-\overline{vw}$	20 minutes $-\overline{uw}$	20 minutes $-\overline{vw}$
2	−0.32	+0.16	−0.55	+0.20	−0.58	+0.20	−0.61	+0.19
4	−0.05	+0.11	−0.18	+0.13	−0.18	+0.14	−0.19	+0.14
8	0.00	+0.16	−0.03	+0.24	−0.04	+0.25	−0.04	+0.25
12	+0.03	+0.12	+0.02	+0.18	+0.04	+0.18	+0.04	+0.19
16	+0.08	+0.16	+0.10	+0.22	+0.12	+0.24	+0.11	+0.26
20	0.00	+0.06	+0.03	+0.11	+0.04	+0.12	+0.04	+0.13
26	+0.01	0.00	+0.02	0.00	+0.02	−0.01	−0.01	0.00
32	0.00	0.00	+0.01	−0.01	+0.02	−0.06	−0.05	−0.03

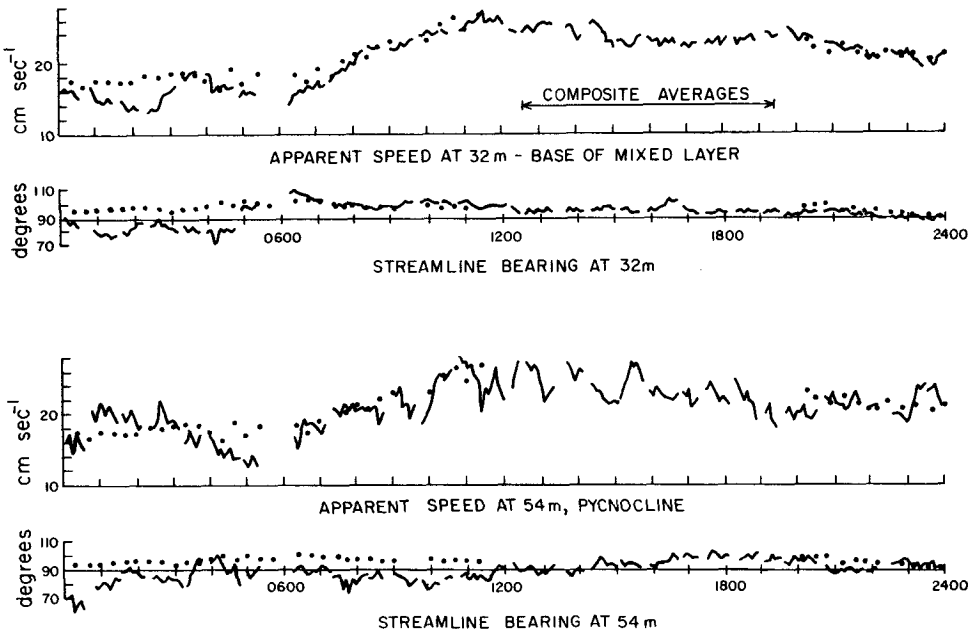

FIG. 6. Relative currents at 32 and 54 m on 12 April 1972: broken lines, currents measured relative to ice; dots, apparent bottom speed and bearing from smoothed acoustic bottom reference data. Time is Alaska Standard.

7. The friction velocity u_*

At the outset, we make a distinction between the skin friction ρu_*^2 which we might expect to measure as the Reynolds stress in the surface layer and τ_0 the total stress over a representative area including form drag effects. For a horizontally homogeneous surface the two would coincide, but in general $\tau_0=\rho u_*^2+\tau_b$ is the stress we would use, e.g., in a regional momentum balance where τ_b is the average form drag force per unit area. Thus, when we speak of u_* we are referring to the proper scaling velocity for the turbulent flow, not necessarily equal to $(\tau_0/\rho)^{\frac{1}{2}}$.

Using the primary composite data listed in Table 3 we see that at 2 m there is appreciable turning of the horizontal stress vector so that we are apparently beyond the surface or constant flux layer. The modulus of the stress at 2 m, 0.67 dyn cm^{-2}, sets a lower bound on u_*^2.

a. *The law of the wall*

There is evidence from numerous experiments and also from scaling considerations (e.g., Blackadar and Tennekes, 1968) that in the neutral atmosphere the law of the wall [(4)] is valid for some distance above the surface layer. Applying (4) to mean velocities at 2 and 4 m yields

$$u_*=k(U_4-U_2)/\ln 2.$$

From Table 3 with $k=0.35$, u_* is equal to 1.1 cm s^{-1}. Clearly this method will reflect any uncertainty in k. We also have no assurance that (4) is valid out to 4 m. In fact, with $u_*=1.1$ the dimensionless height fz/u_* at

TABLE 3. Primary composite average of 5 h of data taken during the period 1230–1930 AST 12 April 1972.

Depth (m)	Speed (cm s^{-1})	Bearing (deg)	U (cm s^{-1})	V (cm s^{-1})	$-\overline{uu}$	$-\overline{vv}$	$-\overline{ww}$	$-\overline{uv}$	$-\overline{uw}$	$-\overline{vw}$	$\lvert\tau\rvert$* (dyn cm^{-2})
							(cm^2 s^{-2})				
2	19.53	73.0	19.53	0.00	−4.30	−1.37	−1.14	−0.35	−0.58	+0.33	0.67
4	21.78	74.7	21.77	−0.66	−1.96	−1.01	−0.57	−0.02	−0.19	+0.25	0.33
8	22.95	74.4	22.94	−0.54	−1.30	−1.09	−0.58	−0.11	+0.08	+0.43	0.44
12	23.48	74.4	23.48	−0.58	−1.15	−0.87	−0.62	−0.17	+0.02	+0.29	0.29
16	23.24	75.8	23.22	−1.14	−1.15	−1.21	−0.65	−0.15	+0.06	+0.39	0.39
20	23.75	79.4	23.60	−2.63	−0.97	−1.28	−0.54	−0.01	+0.02	+0.33	0.33
26	24.17	88.0	23.34	−6.25	−0.83	−0.91	−0.55	−0.55	+0.13	+0.23	0.26
32	23.62	96.7	21.64	−9.47	−0.46	−0.37	−0.31	+0.01	+0.07	+0.05	0.09

* $\lvert\tau\rvert$ is the modulus of the horizontal Reynolds stress.

TABLE 4. Composite average of 8 h data taken during the period 1300–2230 AST 11 April 1972.

Depth (m)	Speed (cm s^{-1})	Bearing (deg)	U (cm s^{-1})	V (cm s^{-1})	$-\overline{uu}$ (cm^2 s^{-2})	$-\overline{vv}$ (cm^2 s^{-2})	$-\overline{ww}$ (cm^2 s^{-2})	$-\overline{uv}$ (cm^2 s^{-2})	$-\overline{uw}$ (cm^2 s^{-2})	$-\overline{vw}$ (cm^2 s^{-2})	$\lvert\tau\rvert$* (dyn cm^{-2})
2	14.01	70.4	14.01	−0.00	−1.64	−0.55	−0.63	−0.12	−0.41	+0.06	0.41
4	15.01	72.6	15.00	−0.59	−0.95	−0.42	−0.29	+0.02	−0.15	+0.11	0.19
8	16.08	72.5	16.07	−0.59	−0.55	−0.36	−0.22	0.00	−0.01	+0.13	0.13
12	16.73	73.4	16.70	−0.89	−0.36	−0.28	−0.22	−0.01	−0.01	+0.08	0.08
16	16.45	77.0	16.34	−1.89	−0.35	−0.44	−0.19	−0.04	+0.04	+0.12	0.13
20	16.25	84.6	15.75	−4.00	−0.27	−0.41	−0.13	−0.03	+0.02	+0.07	0.07
26	15.65	92.8	14.47	−5.94	−0.13	−0.19	−0.06	0.00	+0.02	+0.01	0.02
32	16.32	96.2	14.67	−7.16	−0.09	−0.23	−0.05	0.00	+0.01	+0.01	0.01

* $\lvert\tau\rvert$ is the modulus of the horizontal Reynolds stress.

4 m is about 0.05. Tennekes (1973) suggests that an upper limit for the validity of (4) in the atmosphere is $fz/u_*=0.03$; thus there is little reason to presume that it holds to 4 m. Therefore, we did not place much confidence in this result, although it turned out to be close to the value finally accepted.

b. *The momentum integral*

With the intent of integrating the defect law components (3) we can define the functions $M_y(z)$ and $M_x(z)$ such that

$$M_y(z)=\int_0^z [V(z')-V_R]dz',$$

$$M_x(z)=\int_0^z [U(z')-U_R]dz'.$$

We can then integrate (3) from the surface to some level z to obtain

$$\left.\begin{aligned} -fM_y(z)&=-\overline{uw}(z)+u_*^2+\int_0^z F_x dz' \\ fM_x(z)&=-\overline{vw}(z)+\int_0^z F_y dz' \end{aligned}\right\}, \qquad (11)$$

where F_x and F_y include such effects as advective accelerations and local pressure gradients.

If we can ignore F_x and F_y and find or postulate a level at which the stress vanishes, (11) furnishes an estimate of u_* from the mean velocity profile in the outer layer (Hunkins, 1975). Alternatively, $-\overline{uw}$ can be measured at some point, M_y evaluated at that point, and u_*^2 calculated according to the first equation in (11). Table 5 shows the numerical integration of fM_y for the data from Table 3, along with $-\overline{uw}$. Eq. (11) states that if F_x is ignored, the sum at each level of the last two columns in Table 5 should be $-u_*^2$. Clearly there is a discrepancy: for example, a combination of mean and turbulent measurements at 2 m implies $u_*^2=0.84$ cm^2 s^{-2}; at 4 m it yields $u_*^2=0.71$ cm^2 s^{-2}; and at 32 m (essentially the integral of the mean lateral velocity through the mixed layer) it yields about 2.9 cm^2 s^{-2}. To use Reynolds stress measurements to evaluate u_*^2 from (11) we need to investigate F_x.

c. *A nonhomogeneous estimate*

In order to estimate the magnitude of the topographic force field, F_x, we can find the difference in its integrated effect at two levels by considering directly measured quantities. Let

$$\mathfrak{F}_x(z)=\int_0^z F_x(z')dz',$$

and rewrite the first of (11) as

$$\mathfrak{F}_x(z)+u_*^2=-[fM_y(z)+-\overline{uw}(z)].$$

Then we can estimate $\bar{F}_x$ between levels from $\Delta\mathfrak{F}_x(z)=\bar{F}_x\Delta Z$. These calculations are summarized in Table 6. This technique cannot give an estimate of the value of F_x in the upper 2 m, but we reason that it is set up by some large-scale inhomogeneity and does not vary rapidly near the surface. Thus we can calculate u_*^2 under three different assumptions: 1) treat F_x as constant from 0 to 3 m; 2) decrease F_x linearly from its value at 3 m to 0 at the surface; 3) extend F_x to the surface with the slope given by its values at 3 and 6 m. The corresponding values for u_*^2 (cm^2 s^{-2}) are 0.97, 0.9 and 1.1. Thus we chose $u_*^2=1.0\pm0.1$ as the best estimate. In the next section the square root of this value will be used as the scaling velocity, giving results consistent with our expectations.

The force field F_x is in all likelihood a manifestation of form drag. It has the interesting feature of being balanced geostrophically by a lateral velocity component deep in the boundary layer. Thus, whereas we often think of the outer atmospheric boundary layer (which, by our choice of reference, we are modeling) as a three-way balance between a large-scale pressure gradient, a turbulent stress gradient and the Coriolis force, we see here that a fourth term, probably a

TABLE 5. Momentum integral calculations for lateral component.

Depth (m)	$V - V_R$† (cm s^{-1})	$\overline{(V - V_R)}$	$\overline{(V - V_R)}\Delta z$ (10^2 cm^2 s^{-1})	$fM_y(z)$‡ (cm^2 s^{-2})	$-\overline{uw}$§
0	+9.47*			0	
		9.47	−18.9		
2	+9.47			−0.26	−0.58
		9.14	−18.3		
4	+8.81			−0.52	−0.19
		8.87	−35.4		
8	+8.93			−1.02	+0.08
		8.91	−35.6		
12	+8.89			−1.52	+0.02
		8.61	−34.4		
16	+8.33			−2.00	+0.06
		7.58	−30.4		
20	+6.84			−2.43	+0.02
		5.03	−30.2		
26	+3.22			−2.85	+0.13
		1.61	−07.2		
32	0			−2.95	+0.07

* No turning in upper 2 m is assumed.
† V_R is reference lateral velocity at 32 m.
‡ $M_y(z) = \int_0^z [V(z') - V_R]dz'$.
§ Measured momentum flux values from Table 3.

combination of advective accelerations and local pressure gradients, causes a large distortion of the entire velocity profile, even though the local topographic variations are less than 10% of the layer (see Fig. 3). This will be discussed further in subsequent sections.

8. Nondimensional profiles

With $u_* = 1$ cm s^{-1}, the scaling length u_*/f is about 70 m. Figs. 7–10 show theoretical predictions from various models as solid or dotted lines; solid markers represent measured values nondimensionalized by u_* and u_*/f. Curves from Businger and Arya's (1974) K model are drawn because we wished to show what might be expected for slightly stable conditions. The first stable case they treat is $\mu_* = 10$. There is very little difference among the various models discussed in Section 4 for the neutral PBL, with the exception of turbulent variances, which the K model does not predict at all; curves from both Deardorff (1972) and Wyngaard *et al.* (1974) are shown for these.

Fig. 7 depicts the mean downstream current. Flow in the surface layer is a strong function of Ro_* and at

TABLE 6. Local topographic force field and associated geostrophic flow component V_L.

Depth	Δz	$\mathcal{F}_x(z) + u_*^2$	$\Delta\mathcal{F}_x$	$\bar{F}_x$ ($\times 10^4$)	V_L	v_E
0						
	−200					
2		+0.84				
	−200		−0.13	+ 6.5		
4		+0.71			−0.3	9.1
	−400		+0.23	−5.8		
8		+0.94			+7.1	1.8
	−400		+0.56	−14.0		
12		+1.50			+8.5	0.4
	−400		+0.44	−11.0		
16		+1.94			+8.4	0
	−400		+0.50	−12.5		
20		+2.41			+6.3	0.5
	−600		+0.31	−5.2		
26		+2.72			+2.8	0.4
	−600		+0.15	−2.5		
32		+2.87				

Note: v_E is an estimate of the flow that balances the stress gradient. All derived quantities in cgs units.

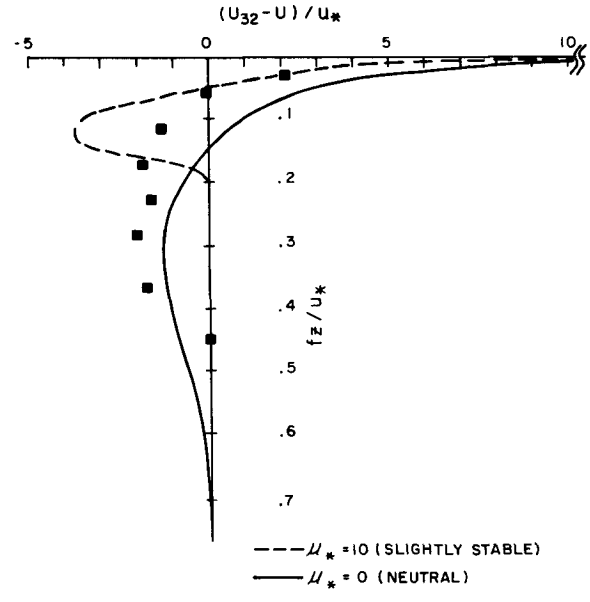

FIG. 7. Nondimensional downstream component with respect to 32 m reference. Curves are model predictions from Businger and Arya (1974). Solid markers are experimentally determined values.

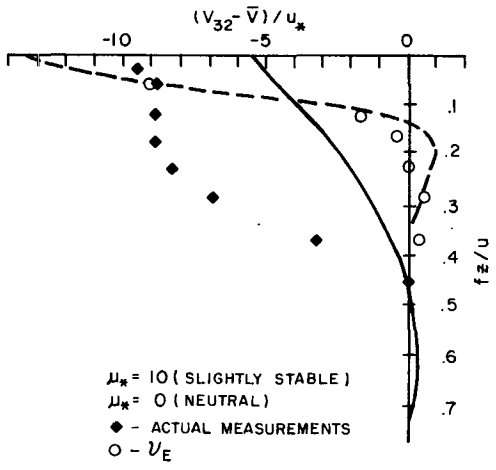

FIG. 8. As in Fig. 7 except for the lateral component.

the surface has the value U_R/u_* of about 22, although this is not shown because the plot is truncated. For the Wyngaard model the surface value is 32 with $\mathrm{Ro}_* \approx 10^7$. Shir (1973) carried Ro_* as a variable and found $U_R/u_* = 24$ with $\mathrm{Ro}_* = 10^5$. Evaluating z_0 from (4) with the mean flow at 2 m yields $\mathrm{Ro}_* \approx 4 \times 10^4$, which is consistent with the value we found for U_R/u_*.

Fig. 8 shows the lateral velocity profile's departure from ideal discussed in Section 7 and attributed to topographic effects. The open circles represent v_E/u_*, where v_E is that part of the lateral component required to geostrophically balance the stress gradient. Considered together, Figs. 7, 8 and 9 demonstrate well the coupling between the stress gradient, the form drag force **F** and the Coriolis force. Clearly the $\overline{uw}$ gradient alone is not sufficient to balance the downstream Coriolis force associated with the V component. On the other hand, measured $\overline{vw}$ and U profiles are comparatively close to their horizontally homogeneous models, indicating that the lateral component of **F** is not important in that balance. Thus **F** seems to be clearly related to the direction of ice stress, and it is natural to assume it to be a local manifestation of form drag.

Fig. 10 shows dimensionless variances, the sum of which is twice the turbulent kinetic energy. Curves from Deardorff's model seem to show more of the observed structure than the simpler second-order model. The reason that the energy levels deep in the layer are higher than predicted might be that the system is affected by an active pycnocline rather than being confined by a rigid lid.

The fact that the $\overline{uw}$ profile falls off rapidly implies that the water column is stable. However, close inspection of the other turbulent quantities seems to refute this. For instance, it is difficult to see why the $\overline{vw}$ and particularly the $\overline{w^2}$ profiles should not also be squeezed in the vertical by a significant buoyant force field. In both cases the measurements follow neutral models.

Some insight into the interaction between the local pressure force F_x and the turbulent stress might be gained from the following simple argument. We usually picture the turbulent momentum transfer as a process whereby a parcel of fluid at one level in a shear flow is swept to a different level by a turbulent eddy, causing a momentum exchange between the two levels, the sign depending on the mean velocity gradient. In a stable environment, the eddy must work against a buoyant force in the vertical and the $\overline{uw}$ or $\overline{vw}$ covariance at increasing depths is diminished, thus steepening the nondimensional gradients. From the mean lateral velocity in our case, we infer a force field in the x direction with a strong negative gradient from 3 to 10 m depth (see Table 6). Thus a downward moving parcel feels an increasing force in the negative x direction against which it must work, with the same result as if the environment were stable. The lateral $\overline{vw}$ transfer will not be much affected, as the measured profile confirms. We have little feeling for how the third independent stress $\overline{uv}$ should behave in a rotating layer, but this same mechanism could serve to diminish its magnitude quickly in the upper layers as the data indicate. By simplifying the covariance equations as much as possible but retaining terms like the velocity-horizontal pressure gradient covariances, one can arrive at similar qualitative conclusions (McPhee, 1975), mainly because the pressure-velocity covariance in the x direction plays a major role in the $\overline{u^2}$ equation, but is felt in the $\overline{v^2}$ equation only through the rotation terms. We thus assert that the flattening of the $\overline{uw}$ stress profile is due to the topographic force, and that the so-called mixed layer is indeed well mixed and near to being dynamically neutral.

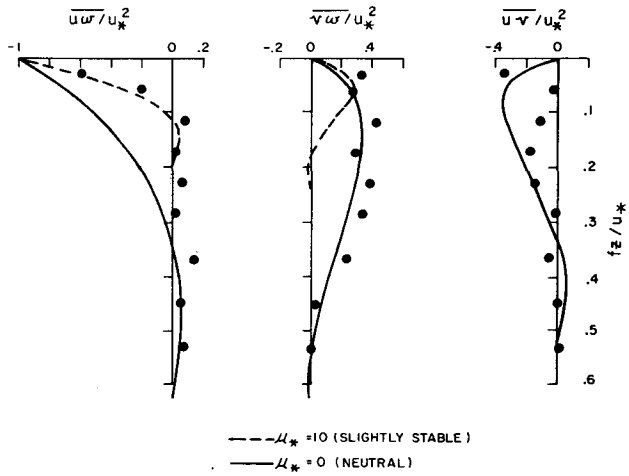

FIG. 9. Nondimensional shear stress. Curves are from Businger and Arya (1974) except $\overline{uv}/u_*^2$ from Wyngaard *et al.* (1974).

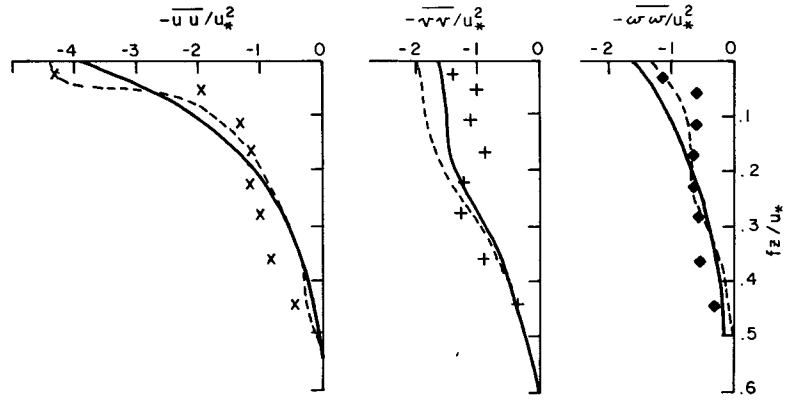

FIG. 10. Nondimensional variances: solid lines, neutral case from Wyngaard *et al.* (1974); dashed lines, neutral case from Deardorff (1972).

Figs. 11 and 12 compare the nondimensionalized profiles for the case we have been discussing (labeled B), with those taken on 11 April (labeled A) and summarized in Table 4. For the latter case, the average reference speed was 16.32 cm s^{-1} with $u_*^2 = 0.7$ cm^2 s^{-2}. Current direction was almost the same in each case. One feature we consider particularly significant is the lower part of the V profile. For Case A ($u_* \approx 0.8$) the pycnocline starts at $\xi = fz/u_* = 0.6$ while for Case B it occurs at $\xi = 0.5$. In each case, the profile swings back to zero at about $\xi = 0.4$ or 0.5, indicating that the force field distorting the lower part of the profile is responding to the same scaling as the rest of the boundary layer rather than, say, to the mixed layer depth. In other words, Figs. 11 and 12 suggest that in the *dimensional* vertical coordinate there was an increase in the depth of the frictional boundary layer from Case A to Case B, despite the fact that the average density structure was much the same on the two days. Although the spacing of the instruments precludes very exact determination of the boundary layer depth, the

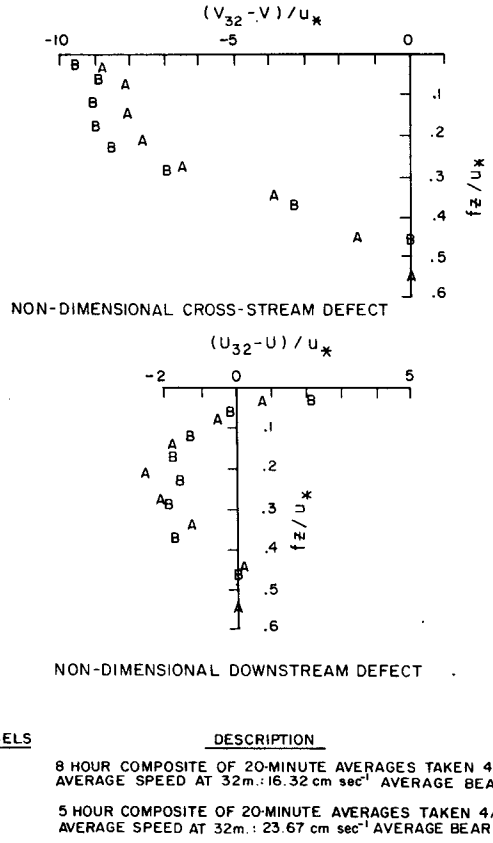

FIG. 11. Comparison of nondimensional mean flow profiles for composite flows of different magnitude.

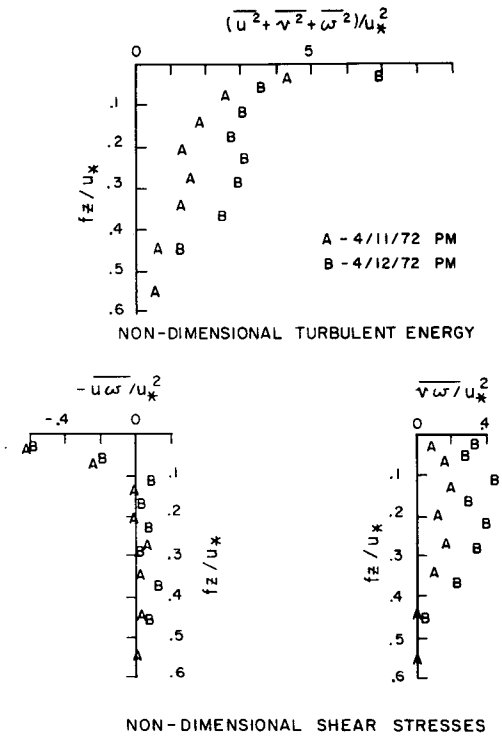

FIG. 12. Comparison of nondimensional turbulent energy and shear stress profiles for composite flows of different magnitude.

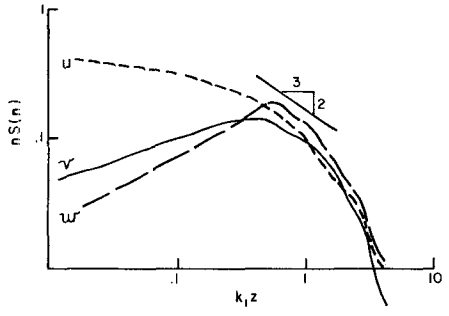

FIG. 13. Spectra of downstream u, lateral v and vertical w velocity fluctuations for first triplet below ice at 2 m.

turbulence in Case A seems to have died off around 26 m (the second data point from the bottom), while the mixed (isopycnal) layer was about 38 m deep. This, of course, implies that u_*/f, as well as the total depth of the mixed layer, is an important parameter in turbulent entrainment processes.

Within the resolution provided by our instrument spacing, both the mean flow and turbulent energy profiles in Figs. 11 and 12 indicate that the depth of frictional influence lies in the range $0.4<\xi<0.5$, in good agreement with most recent neutral PBL models (e.g., see Shir, 1973).

The results presented in this section indicate that the boundary layer does respond to neutral PBL scaling. They show, also, that although topography apparently has a severe effect on the mean profile, its influence on the turbulent structure is relatively small. We point out that this system is a scale model of the atmospheric PBL and suggest that perhaps topography affects wind profiles farther aloft than commonly thought.

9. Turbulence spectra

Spectral analysis of the turbulent velocity fluctuations was aimed at (i) determining if our current measurement system had the response necessary to measure turbulence adequately and (ii) seeing if spectra could further elucidate the physical processes in the outer PBL.

Throughout the following analysis we have made liberal use of Taylor's hypothesis, i.e., we considered our probes as being dragged through a "frozen" turbulent field with spatial changes related to temporal changes by the mean flow speed (Lumley and Panofsky, 1964). With maximum turbulent intensities $\overline{q^2}/U^2$ of about 2%, this seemed justified, especially for higher frequencies.

Spectra were calculated for each triplet in the mixed layer according to the following scheme:

1) A time series of $N=1024$ points was formed by block averaging eight sample points corresponding to a time step of $\Delta t=1.62$ s.

2) An average streamline reference frame was determined by rotating the V and W (average) components to zero. Each point in the series was rotated into this frame and the mean speed U was removed leaving three series of fluctuating components, all with zero mean: downstream u, lateral v and vertical w.

3) Each series was discrete-Fourier transformed and the spectral estimate $S(n)$ calculated by taking the absolute square of the transform.

4) Each spectral estimate was multiplied by its index n and classified in wavenumber bands according to the log of its dimensionless wavenumber $kz=nz/(N\Delta tU)$.

5) Thirty runs, picked from reasonably steady periods during the storm of 11–13 April, were accumulated, averaged and plotted $\log[nS_\alpha(n)/\sigma_\alpha^2]$ against $\log kz$, $\alpha=u, v, w$, for each level in the mixed layer.

The weighted spectral estimate $nS(n)$ rather than $S(n)$ was chosen to conform to atmospheric spectral studies (e.g., Panofsky and Mazzola, 1971) and for convenience (the ordinate is independent of abscissa units). The log-log plot rather than the "area-preserving" plot was used to better display the slopes of the spectra. For lower frequencies the number of samples in each wavenumber band was comparatively small with correspondingly large variance. A smooth curve was drawn by eye to estimate the spectrum, but only for wavenumbers less than the peak in the w spectrum. Figs. 13, 14 and 15 show the results of this procedure for the levels, 2, 4 and 8 m from the ice, respectively.

Fig. 13 answers the first question posed in this section. The dimensionless cutoff wavenumber corresponding to the distance through which the rotor must travel to make one revolution ($\sim$8 cm) for the triplet at 2 m is about 3.2, when the angle of attack is considered (McPhee, 1975). Information about disturbances with wavenumbers greater than this will be affected by the geometry of the experimental probes, but it is clear that nearly all the energy is in wavenumbers <3.2. Since this wavenumber cutoff is lower than the cutoff imposed by the dynamical response of the rotors (Smith, 1974a), we conclude that the instruments did measure the energy-containing range of the turbulent flow field. Examination of the shifts in the spectra at 4 and 8 m in Figs. 14 and 15 shows that 2 m is the critical case, as we would expect.

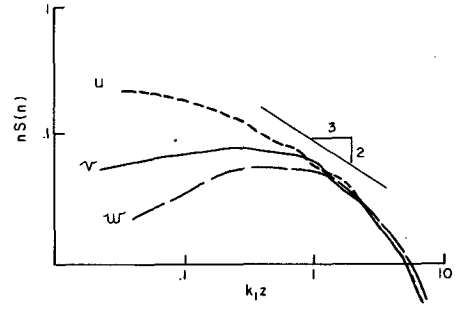

FIG. 14. Spectra of velocity fluctuations for second triplet, 4 m below ice.

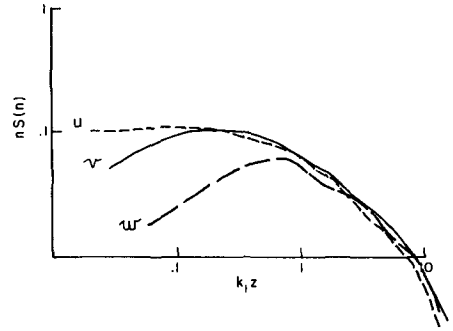

FIG. 15. Spectra of velocity fluctuations for third triplet, 8 m below ice.

From turbulence spectral theory we expect any turbulent spectrum to become essentially isotropic and homogeneous at high wavenumbers and under those circumstances a fairly simple relationship holds between the true (three-dimensional) turbulent spectrum and the spectrum measured along one axis using Taylor's hypothesis (Bathelor, 1953). In addition, if the Reynolds number based on turbulent length and velocity scales of the flow is high enough, there exists along the wavenumber axis a region called the inertial subrange for which the flow is also independent of viscosity. For this range the longitudinal spectrum is

$$F(k_1) = a_1 \epsilon^{2/3} k_1^{-5/3},$$

where k_1 is the wavenumber along the longitudinal axis and ϵ the dissipation rate. Also, the ratio of the vertical (and lateral) spectrum to the longitudinal spectrum is 4/3 (Busch *et al.*, 1968). Fig. 13 shows that at 2 m these criteria may be met in a short interval, but for greater depths we suspect that the turbulent Reynolds number becomes too small for a true inertial subrange (Tennekes and Lumley, 1972, p. 266). However, the $-5/3$ slope ($-2/3$ in the weighted representation) is often observed at lower wavenumbers, particularly in longitudinal spectra, and seems to be present at all these depths.

Using $a_1 = 0.15$ as the approximate value of the proportionality constant[2] reported for atmospheric surface layer studies in which shear production is assumed to equal dissipation (Busch and Panofsky, 1968, p. 137), we found from typical values at 2 m that dissipation was about half the shear production. This is consistent with our interpretation of the form drag force discussed in Section 7, where we asserted that turbulent eddies would have to do work against the force gradient in a manner somewhat analogous to work done in a stable environment with the flux Richardson number less than critical.

Fig. 16 shows normalized spectra of vertical velocity fluctuations at all levels in the mixed layer. With the exception of 32 m, the spectra are of similar shape, but show a rightward shift of the dimensionless peak with increasing depth. The spectrum at 32 m may be different because of its proximity to the pycnocline, where other processes were occurring.

The wavelength λ_m at which the peak in the spectrum occurs is indicative of a length scale for the large, or "energy-containing," eddies. In the neutral surface layer, we expect the scaling to be proportional to z; therefore, the dimensionless peaks should coincide. As we get farther from the boundary, the dominant eddy scale is no longer proportional to z and we expect the peaks to shift rightward with increasing depth, as observed. If the mixing length and therefore K were constant, the rightward shift should be proportional to the change in depth. If we express the eddy viscosity as proportional to $u_*\lambda$ rather than u_*z, i.e.,

$$K = c_1 u_* \lambda_m,$$

then Fig. 16 suggests a K distribution. It remains only to evaluate c_1 at one location. By assuming that the logarithmic profile is reasonably valid to 2 m (an assumption we considered somewhat justified from the fact that u_* calculated from mean velocities at 2 and 4 m is quite close to the value determined from flux measurements), we can find c_1 from measurements at 2 m only by the relationship

$$K\frac{\partial U}{\partial z} = -\overline{uw},$$

from which

$$K = -\overline{uw}kz/u_* = c_1 u_* \lambda_m.$$

For typical conditions this yields $c_1 = 0.1$.

From the spectra in Fig. 16 it is evident that in some cases a peak is hard to identify, so we reasoned that

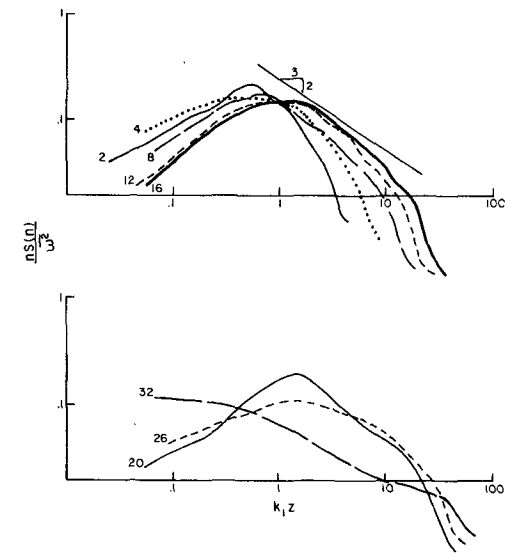

FIG. 16. Normalized vertical spectra at eight levels in the mixed layer. Numbers are depths in meters.

[2] This is equivalent to a value of 0.51 for the Kolmogorov constant α_1, where the wavenumber is defined by $\kappa = 2\pi k_1$.

TABLE 7. K distribution based on peaks in vertical spectra.

Depth	$\log z/\lambda_m$	λ_m(m)	fz/u_*	Kf/u_*^2 ($\times 10^3$)
2	−0.30	4.0	0.03	5.9
4	−0.07	4.7	0.06	6.9
8	−0.03	8.6	0.11	12.6
12	+0.18	7.9	0.17	11.6
16	+0.33	7.5	0.22	11.0
20	+0.30	10.0	0.28	14.7
26	+0.83	3.9	0.37	5.7
32	+1.52	1.0	0.45	1.5

choosing a point where each spectrum first matched a straight chord with $-2/3$ slope would provide a consistent estimate of the characteristic wavelength. This procedure was carried out for typical conditions and is summarized in Table 7. This entails some subjectivity on the part of the observer and should be considered a rough estimate only. The values are plotted in Fig. 17 along with K curves from Businger and Arya (1974) and Deardorff's (1972) longitudinal austausch coefficient. We wish to stress that K in the horizontally homogeneous models is a ratio of turbulent stress to mean wind shear, while in our case it is proportional to the dominant eddy size, with the proportionality constant determined from surface layer arguments. It is clear from Figs. 7–9 that no simple relationship exists between the stress components and the product of this eddy viscosity and mean shear. It is interesting, though, that the vertical size of dominant eddies is apparently not much affected by the force that distorts the V profile and flattens the longitudinal stress profile.

Incidentally, if we calculate K from the usual definition of the Ekman depth in the simple constant-K treatment

$$K = fD^2/2\pi^2$$

with $D = 32$ m as our reference depth, the nondimensional value is $fK/u_*^2 = 0.01$, which fits in reasonably well with values at depths >4 m.

10. Conclusions

In this paper we have presented what we believe to be the first published measurements of mean current and turbulent stress made simultaneously at several levels throughout an entire PBL. Our results were as follows:

1) The mixed layer coincided closely with the frictional boundary layer observed during *maximum* ice speeds and was nearly neutrally stable. This was confirmed by direct measurements and inferred from the dynamical response of the turbulent flow.

2) The friction velocity was best determined from momentum flux measurements and consideration of the mean momentum equation with an estimate of the effect of topography. This value agreed reasonably well with the value found by assuming a logarithmic mean profile to 4 m, but was significantly less than the value obtained from integrating the lateral velocity throughout the whole PBL.

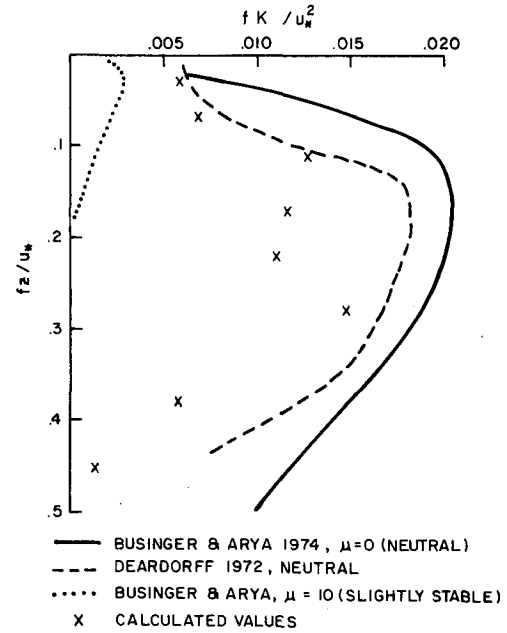

FIG. 17. Nondimensional eddy viscosity. Calculated values are obtained from peaks in vertical spectra.

3) With the important exception of lateral velocity, the profiles of mean current and Reynolds stress, when nondimensionalized by u_* and u_*/f, agreed well with recent atmospheric PBL models.

4) Peaks in the spectra of vertical velocity were used to derive a K (eddy viscosity) distribution from the relation $K \propto u_*\lambda_m$ that agrees fairly well with Deardorff's (1972) distribution. Because of the inviscid topographic force, however, there was no simple relationship between K, $\partial U/\partial z$ and $\overline{uw}$.

Acknowledgments. This work was supported by the Office of Naval Research under Contracts N-00014-67-0103-0021 and N-00014-67-0103-0034 and by AIDJEX.

REFERENCES

Batchelor, G. K., 1953: *The Theory of Homogeneous Turbulence.* Cambridge University Press, 197 pp.

Blackadar, A. K., and H. Tennekes, 1968: Asymptotic similarity in neutral planetary boundary layers. *J. Atmos. Sci.*, **25**, 1015–1019.

Brown, R. A., 1974: *Analytic Methods in Planetary Boundary Layer Modeling.* Adam Hilger, 150 pp.

Busch, N. E., and H. A. Panofsky, 1968: Recent spectra of atmospheric turbulence. *Quart. J. Roy. Meteor. Soc.*, **94**, 132–148.

——, J. A. Frizzola and I. A. Singer, 1968: The micrometeorology of the turbulent flow field in the atmospheric surface boundary layer. *Acta Polytech. Scand.*, **50**, 1–45.

Businger, J. A., and S. P. S. Arya, 1974: The height of the mixed layer in the stably stratified planetary boundary layer. *Advances in Geophysics*, Vol. 18A, Academic Press, 73–92.

——, J. C. Wyngaard, Y. Izumi and E. F. Bradley, 1971: Flux-profile relationships in the atmospheric surface layer. *J. Atmos. Sci.*, **28**, 181–189.

Deardorff, J. W., 1972: Numerical investigation of neutral and unstable planetary boundary layers. *J. Atmos. Sci.*, **29**, 91–115.

Heiberg, A., and R. Bjornert, 1972: Operations and logistics support, 1972 AIDJEX pilot study. AIDJEX Bull., No. 14 (July), 1–11.

Hunkins, K., 1975: The ocean boundary layer and stress beneath a drifting ice floe. *J. Geophys. Res.*, **80**, 3425–3433.

Lumley, J. L., and H. A. Panofsky, 1964: *The Structure of Atmospheric Turbulence.* Interscience, 239 pp.

McPhee, M. G., 1975: An experimental investigation of the boundary layer under pack ice. Tech. Rep. M75-14, Dept. Oceanogr., University of Washington, 164 pp.

Monin, A. S., 1972: *Weather Forecasting as a Problem in Physics.* The MIT Press, 199 pp.

Panofsky, H. A., and C. Mazzola, 1971: Variances and spectra of vertical velocity just above the surface layer. *Boundary Layer Meteor.*, **2**, 30–37.

Shir, C. C., 1973: A preliminary numerical study of atmospheric turbulent flows in the idealized planetary boundary layer. *J. Atmos. Sci.*, **30**, 1327–1339.

Smith, J. D., 1972: Surface boundary layer study. AIDJEX Bull., No. 14 (July), 40–43.

——, 1974a: Turbulent structure of the surface boundary layer in an ice-covered ocean. *Proc. 1973 ICES Symp. Physical Processes Responsible for the Dispersal of Pollutants in the Sea, with Special Reference to the Near Shore Zone.* Rapports et Proces-Verbaux Series, J. W. Talbot and G. Kullenberry, Eds., 55–65.

——, 1974b: Oceanographic investigations during the AIDJEX lead experiment. AIDJEX Bull., No. 27 (November), 125–133.

Tennekes, H., 1973: The logarithmic wind profile. *J. Atmos. Sci.*, **30**, 234–239.

——, and J. L. Lumley, 1972: *A First Course in Turbulence.* The MIT Press, 300 pp.

Welch, M., E. Partch, H. Lee and J. D. Smith, 1973: Diving report, 1972 AIDJEX Pilot Study. AIDJEX Bull., No. 18, (February), 31–44.

Wyngaard, J. C., 1973: On surface layer turbulence. *Workshop on Meteorology*, D. Haugen Ed., Amer. Meteor. Soc., 101–149.

——, O. R. Coté and K. S. Rao, 1974: Modeling the atmospheric boundary layer. *Advances in Geophysics*, Vol. 18A, Academic Press, 193–212.